Title

Imaging the developing human external and internal urogenital organs with light sheet fluorescence microscopy.

Authors

Isaacson, Dylan
McCreedy, Dylan
Calvert, Meredith
et al.

Publication Date

2020

DOI

10.1016/j.diff.2019.09.006

Peer reviewed

Differentiation 111 (2020) 12–21

Contents lists available at ScienceDirect

Differentiation

journal homepage: www.elsevier.com/locate/diff

Imaging the developing human external and internal urogenital organs with light sheet fluorescence microscopy

Dylan Isaacson[a,*], Dylan McCreedy[b], Meredith Calvert[c], Joel Shen[d], Adriane Sinclair[e], Mei Cao[e], Yi Li[e], Todd McDevitt[f,g], Gerald Cunha[e], Laurence Baskin[e,h]

[a] Department of Urology, Northwestern University Feinberg School of Medicine, Chicago, IL, USA
[b] Department of Biology, Texas A&M University, College Station, TX, USA
[c] Histology and Light Microscopy Core, J. David Gladstone Institutes, San Francisco, CA, USA
[d] CytomX Therapeutics, Inc. South San Francisco, CA, USA
[e] Department of Urology, University of California, San Francisco, San Francisco, CA, USA
[f] Department of Bioengineering and Therapeutic Sciences, J. David Gladstone Institutes, San Francisco, CA, USA
[g] Institute of Cardiovascular Disease, J. David Gladstone Institutes, San Francisco, CA, USA
[h] Division of Pediatric Urology, University of California San Francisco Benioff Children's Hospital, San Francisco, CA, USA

ARTICLE INFO

Keywords:
Microscopy
Light sheet fluorescence microscopy
Selective plane illumination microscopy
Genital development
Urogenital development
CLARITY

ABSTRACT

Technological advances in three-dimensional (3D) reconstruction techniques have previously enabled paradigm shifts in our understanding of human embryonic and fetal development. Light sheet fluorescence microscopy (LSFM) is a recently-developed technique that uses thin planes of light to optically section whole-mount cleared and immunolabeled biologic specimens. The advent of commercially-available light sheet microscopes has facilitated a new generation of research into protein localization and tissue dynamics at extremely high resolution. Our group has applied LSFM to study developing human fetal external genitalia, internal genitalia and kidneys. This review describes LSFM and presents our group's technique for preparing, clearing, immunostaining and imaging human fetal urogenital specimens. We then present light sheet images and videos of each element of the developing human urogenital system. To the extent of our knowledge, the work conducted by our laboratory represents the first description of a method for performing LSFM on the full human urogenital system during the embryonic and fetal periods.

1. Introduction

Throughout history, three-dimensional (3D) reconstruction techniques have played an integral role in understanding the intricate mechanisms that underlie human development. In the mid-1800s, embryologic models were painstakingly carved freehand and validated with caliper measurements from histologic sections. In those early days, modeling required collaborations between professional modeler-artists such as Adolf Ziegler and embryologists such as Wilhelm His, the widely-recognized inventor of the microtome (Hopwood, 1999). In the latter half of the 19th century, freehand techniques were largely supplanted by the "plate-modeling method" of Gustav Born. In Born's method, enlarged projections of serial histologic slides were hand-traced onto wax plates and used to produce enlarged 3D reconstructions of embryos at different stages of development by stacking the plates, physically isolating structures of interest and melting them together (Born, 1883). In subsequent years, His's former student Franklin Mall and other anatomists at Johns Hopkins University applied Born's method to perform seminal investigations on human embryos that still form the foundation of our knowledge of human development (Fig. 1). Although newer devices have automated and accelerated 3D reconstruction as compared to technicians tracing and cutting individual wax plates, contemporary methods of 3D reconstruction still rely on the same basic principles of section tomography as those employed in the late 19th century.

In 1903, at the same time Franklin Mall was collecting and modeling human embryos, Henry Sidentopf and Richard Zsigmondy at Carl Zeiss AG first described the ultramicroscope, a device that used sunlight projected through a slit aperture to illuminate individual planar sheets of gold molecules in suspension (Siedentopf and Zsigmondy, 1903). Despite this early innovation, it took nearly a century for light sheet microscopy to become widely applied. In 1993, Voie et al. applied this

* Corresponding author.
E-mail address: Laurence.baskin@ucsf.edu (D. Isaacson).

https://doi.org/10.1016/j.diff.2019.09.006
Received 30 June 2019; Received in revised form 7 September 2019; Accepted 10 September 2019
Available online 10 October 2019

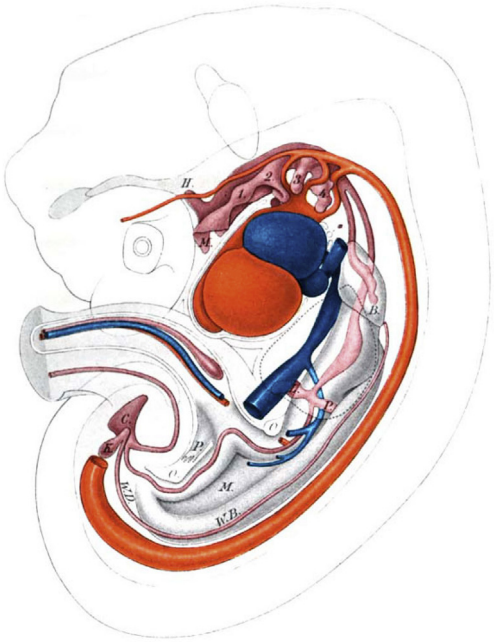

Fig. 1. [26-day old human embryo wax plate] reconstruction viewed from the left side. Enlarged 15 times. H. hypophysis; M. mouth, mesentery; I, 2, 3, 4, branchial pockets; B. bronchus; P. pancreas; L. liver; W.B. Wolffian body; W.D. Wolffian duct; K.kidney; C. cloaca; 0. openings by which the pleuro-peritoneal cavities communicate; P. papilliform projection into the lower opening. *Reproduced from Mall FP. A human embryo twenty-six days old. (1891) Journal of Morphology 5: 459–480. Public domain.*

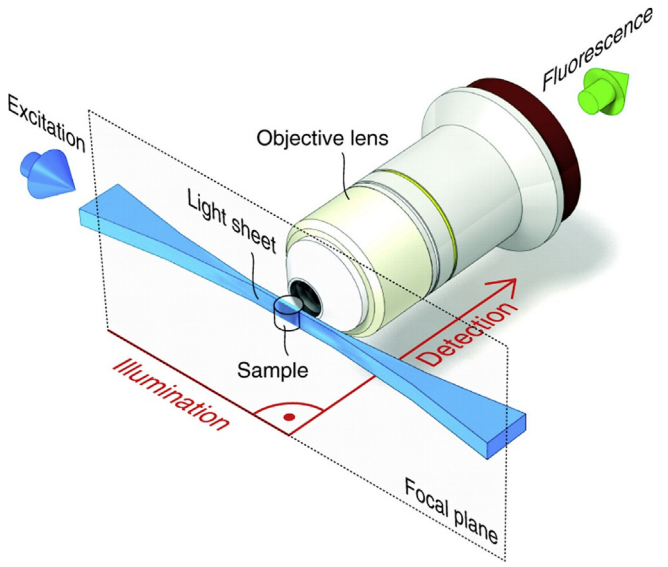

Fig. 2. *The concept behind fluorescence light-sheet microscopy. In light-sheet microscopy, fluorescence excitation (blue arrow) and detection (green arrow) are split into two distinct optical paths. The illumination axis is orthogonal to the detection axis. A microscope objective lens and common widefield optics are used to image the sample onto a camera (not shown). The illumination optics are designed to illuminate a very thin volume around the focal plane of the detection objective. Many different implementations of this principle exist, however, the most common one is the generation of a sheet of laser light that illuminates the sample in the focal plane from one side. Reproduced from Huisken J, Stainer D.Y.., Selective plane illumination microscopy techniques in developmental biology. Development 2009 136: 1963–1975;* https://doi.org/10.1242/dev.022426*, with permission. (For interpretation of the references to color in this figure legend, the reader is referred to the Web version of this article.)*

same principle to optically section fluorescently-labeled hamster cochleae. In their approach, single planes of a specimen to be imaged were individually excited and recorded without interference from out-of-focus elements of their specimens. The aggregated result was a high-resolution 3D reconstruction demonstrating internal and external structures in fine detail. Early microscope prototypes developed by Jan Huisken, Ernst Stelzler (Huisken et al., 2004) and Ulrich Dodt (Dodt et al., 2007) applying these principles refined LSFM technology and culminated in the recent release of several commercially-available devices.

The work presented in this article focuses on one LSFM technique, selective plane illumination microscopy (SPIM). As in Born's original plate-modeling method, SPIM is based on section tomography in which each point in a specimen corresponds to an exact three-dimensional voxel (volumetric pixel) within a reconstructed model. In SPIM, the specimen to be optically sectioned is illuminated from its side by a plane of light emitted by the microscope's illumination objective. The light sheet originates from a laser, the beam of which is collimated and expanded within a beam expander and focused using a cylindrical lens (Santi, 2011). As cylindrical optics result in a concave light sheet, images are recorded at the narrowest point of the light sheet. This is accomplished using a second recording objective, oriented perpendicularly to the illumination objective, which detects fluorescent emissions from the specimen as it is physically translated past the illumination objective (Fig. 2) (Huisken and Stainier, 2009). Fluorescence can be “autofluorescence” from naturally occurring NADH, FAD and other biomolecules (Andersson et al., 1998), from exogenous fluorescent immunolabels or nucleic acid hybridization probes or from endogenously-produced fluorescent proteins (green fluorescent protein and its variants). Commercially-available SPIM devices are able to excite fluorescent tags at multiple wavelengths of visible light enabling co-localization of multiple target proteins in a single specimen.

Regarding specimen positioning for data acquisition, specimens must simultaneously remain within the working distances of both the illumination and recording objectives. This is usually accomplished by immersing the specimen in a small chamber filled with liquid medium at equal distance from all microscope objectives (Adams et al., 2015). For whole-mount specimens, the location of the specimen within the chamber can be manipulated in various ways - via passing a hook through the specimen, fixing it to a rigid rod with an adhesive, or suspending the specimen in a column of translucent agarose (Reynaud et al., 2015). Suspension within agarose results in some degree of diffraction of the light sheet as it passes through, necessitating additional clearing and refractive-index matching steps. This is prevented with using a hook or rod, however these methods render the part of the specimen attached to the hook or rod unable to be imaged and can result in destruction or distortion of the specimen if not performed carefully.

Imaging whole-mount developing fetal organs with LSFM requires excitation of targets in the specimen interior while minimizing absorption and scattering of the light sheet (Richardson and Lichtman, 2015). Therefore, optical clearing of specimens is of great importance. Successful clearing removes light-scattering substances (lipids, water) from the specimen while equilibrating the refractive index of the specimen with the liquid medium within the microscope chamber (Santi, 2011; Richardson and Lichtman, 2015). This has been accomplished in various ways - via normalizing the specimen's refractive index to that of volatile organic solvents (3D Imaging of Solvent-Cleared Organs/3DISCO (Erturk and Bradke, 2013; Erturk et al., 2012)), through dehydration and hyperhydration with aqueous solutions containing mixtures of urea and sugar alcohols (ScaleA2 (Hama et al., 2011), ScaleS (Hama et al., 2015)) or through stabilization of target biomolecules in hydrogel polymers allowing for gentle dissolution of lipids (PAssive CLARITY Technique/PACT, Perfusion-Assisted Release in Situ/PARS (Treweek et al., 2015)). In our laboratory we apply PACT, a technique that allows for excellent transparency and retention of fluorescent

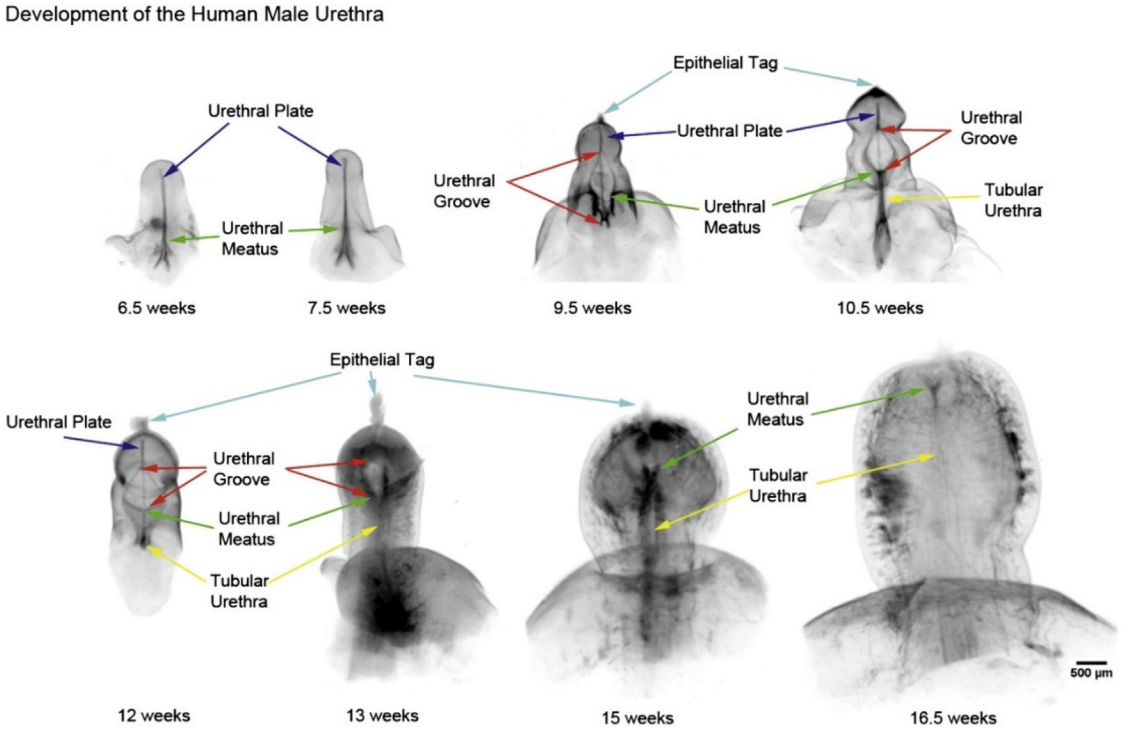

Fig. 3. Optical projection tomography of male urethral development from 6.5 to 16.5 weeks fetal age. Note the progression of the urethral meatus (green arrows) from the level of the scrotal folds at 6.5 weeks to its terminal position at the glans penis at 16.5 weeks. Wide open urethral groove (red arrows) is best seen from 9.5 to 13 weeks with clear progression of proximal to distal fusion of the edges of the urethral groove to form the tubular urethra (yellow arrows). At 13 weeks the urethral groove is within the glans penis with the tubular urethra completely formed within the shaft of the penis. *Reproduced from Li, Y., A. Sinclair, M. Cao* et al.*, Canalization of the urethral plate precedes fusion of the urethral folds during male penile urethral development: the double zipper hypothesis. J Urol, 2015. 193(4): p. 1353-59, with permission.* (For interpretation of the references to color in this figure legend, the reader is referred to the Web version of this article.)

signals while avoiding potential damage to LSFM imaging objectives by organic solvents or to tissues from the contraction and expansion that occurs in hyperhydration-based methods (Richardson and Lichtman, 2015).

Recent investigations by our group employing whole-mount, 3D imaging techniques have elucidated the mechanisms by which the human external genitalia form during the late embryonic and early fetal periods (Li et al., 2015; Overland et al., 2016; Shen et al., 2016; Isaacson et al., 2018a). We recently reviewed the workings and applications of these techniques (Isaacson et al., 2018a). Rather than a simple midline fusion process between two paired shelves as is seen in the palate, the formation of the human penile urethra is much more complex. We have previously used optical projection tomography (OPT) to demonstrate that penile urethral formation involves the distal canalization of the solid endoderm-derived urethral plate within the genital tubercle to form the wide open urethral groove (Fig. 3). This is followed by the subsequent fusion of multiple interlacing ventral epithelial “cords” to form the mature tubular penile urethra (Li et al., 2015; Shen et al., 2016). As described prior, SPIM has since supplanted the use of OPT in our laboratory (Isaacson et al., 2018a). We have applied SPIM to validate our OPT-derived observations, demonstrating that cytokeratin 7 is expressed circumferentially in the urothelium of the nascent penile tubular urethra and illuminates the actively fusing epithelial cords of the urethral folds (see Results section). Though recent work has presented LSFM images of internal human fetal urogenital organs (Belle et al., 2017), we believe the new and previously described findings presented in this review represent the first application of LSFM/SPIM to image the developing human external genitalia and the urogenital system in its entirety. The speed with which LSFM devices acquire data, the high resolution of the resulting images and the ability to re-stain and re-image individual specimens make LSFM/SPIM a powerful new tool for researchers to investigate human development.

2. Materials and methods

2.1. Specimen acquisition

Human fetal urogenital specimens were obtained with approval from the institutional review board (IRB) at the University of California, San Francisco (UCSF). The collection technique has been described previously (Cunha et al., 2016). In the majority of cases, we were able to locate human fetal kidneys, bladders, prostates, gonads, female and male reproductive tracts and external genitalia (Fig. 4). We transported the depicted organs to our lab in 4 °C phosphate-buffered saline (PBS) or RPMI medium (UCSF Cell Culture Facility, San Francisco, CA), separated them from the surrounding connective tissue under a dissecting microscope (Zeiss Stemi-2000-C, Carl Zeiss Ag, Oberkochen, Germany) and photographed them with the digital recording element of the microscope. Specimen age was estimated using heel-toe length (Drey et al., 2005) and genetic sex was determined by polymerase chain reaction (PCR) of the sex-determining Y region (SRY) gene, morphology of Wolffian and Mullerian structures and/or by the presence of testes and ovaries.

2.2. Fixation and storage

In order to stabilize tissues to maintain their integrity and preserve molecular targets during passive clearing, organs need to be perfused with a crosslinking fixative agent (Treweek et al., 2015; Tomer et al., 2014). Our specimens were fixed in 4% paraformaldehyde (PFA) at room temperature for 2–3 h. This short fixation time helps prevent excessive crosslinking precluding satisfactory clearing. We have also achieved good imaging results with small (< 8 mm) organs previously fixed with 10% neutral buffered formalin and stored for months to years in 70% ethanol, although these took longer to clear sufficiently

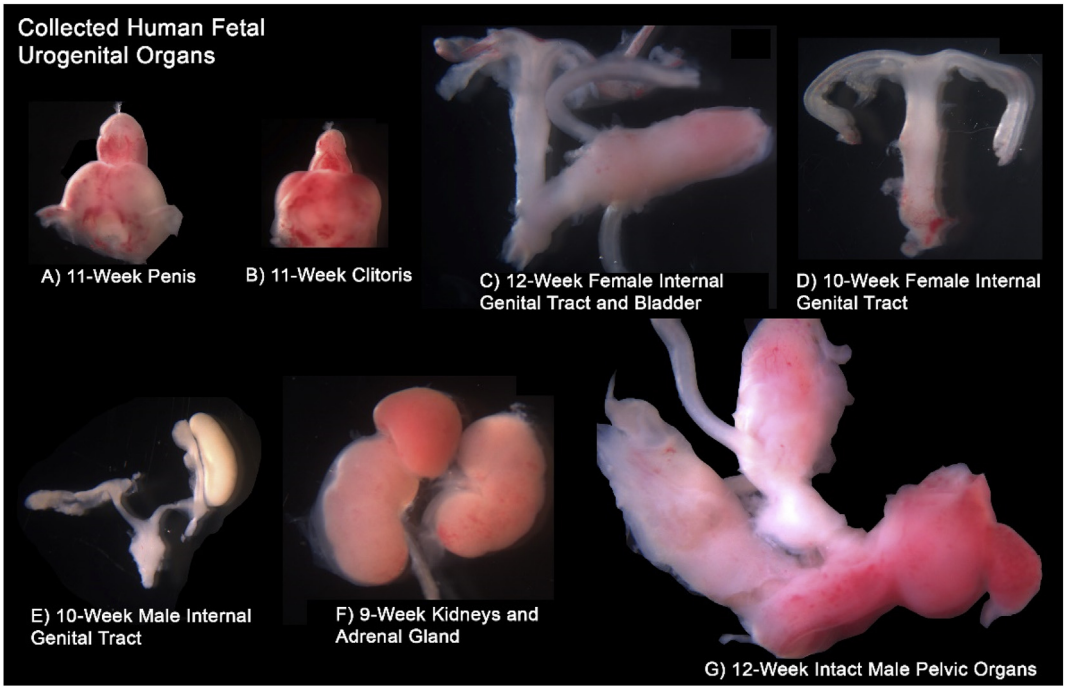

Fig. 4. Human fetal urogenital specimens following collection and dissection demonstrating male and female external genital organs (A, B), male and female internal genital tracts (C, D, E), urinary organs (F, G) and adrenal gland (F).

for optical sectioning than less extensively crosslinked tissues.

To optimize workflow in whole-mount immunostaining and LSFM imaging, we immunostained multiple organs collected at different times in parallel. Organs preserved with 4% PFA were stored in sterile PBS at 4 °C until ready for whole-mount immunostaining. We successfully imaged organs stored for up to a month in this fashion.

2.3. Hydrogel tissue stabilization

We applied the PAssive CLARITY Technique (PACT) to prepare specimens for imaging (Treweek et al., 2015). Native targets of immunostaining were stabilized in a supporting matrix of polymerized acrylamide, allowing for dissolution of lipids without loss of target biomolecules (Tomer et al., 2014). The initiation of acrylamide polymerization to form a solid hydrogel was accomplished via a water-soluble azo initiator that decomposes to form free radicals at elevated temperatures (Chung et al., 2013) (VA-044, Wako Chemicals USA Inc., Richmond, VA). 4% PFA-fixed specimens were washed in sterile PBS with 2–3 buffer changes and transferred to a 4 °C solution of 4% acrylamide in PBS supplemented with 0.25% thermoinitiator for 12–24 h. Unpolymerized acrylamide is highly toxic and carcinogenic so we performed batch-preparation of acrylamide-thermoinitiator solution in a ducted fume hood and froze aliquots at −18 °C until needed.

After 12–24 h at 4 °C in the acrylamide-thermoinitator solution, organs need to be degassed to remove ambient oxygen molecules that would otherwise inhibit free radical polymerization via acting as a free radical trap (Menter). We accomplished this via covering the aliquot container containing the organ and the acrylamide solution with two layers of Parafilm (Bemis N.A., Neenah, WI), inserting a long needle into the bottom of the container and gently bubbling nitrogen gas into the solution for 1–5 min. Following this, we placed the container into a 37 °C incubator for 2–3 h to initiate thermoinitiator degradation and free radical-induced polymerization. Following 2–3 h of 37 °C incubation, organs were removed from the solution and washed in PBS at room temperature with 2–3 PBS changes to remove excess hydrogel before clearing.

2.4. Clearing

Lipids were gently dissolved from hydrogel-bound specimens to enhance their transparency. Specimens were immersed in 50 ml conical tubes filled with a detergent, 8% sodium dodecyl sulfate (SDS), in PBS and incubated at 37 °C with gentle agitation for 2–14 days. The length of time required to attain tissue transparency varies with several factors. These include the size of the tissue, the density of tissue as a function of fetal age, epithelialization of the organ (external organ vs. internal organ) and the extent of crosslinking induced during tissue fixation. Achieving optimal transparency is balanced with preventing detergent-induced damage to fragile superficial structures such as the epithelial tag of the developing glans penis and the urethral/vestibular folds. When our specimens were rendered transparent, we removed them from the clearing solution and washed them in room-temperature PBS with 2–3 PBS changes in preparation for immunostaining (Fig. 5). Specimen clearing can be accelerated through the use of electrophoretic devices (Hockendorf et al., 2014), although we do not yet regularly apply these techniques in our laboratory.

2.5. Antibody staining

Specimens ready for staining were immersed in blocking buffer (Super Block, Thermo Fisher Scientific, Waltham, MA) for 12–24 h to reduce background fluorescence from nonspecific antibody binding. Laser illumination with the light sheet microscope allows for excitation of up to five fluorophores, thus multiple antibodies can be applied to a single specimen as long as each has a species-specific secondary antibody conjugated to a fluorophore of a distinct wavelength. Primary antibodies were diluted in blocking buffer and cleared specimens were immersed in this solution at room temperature with gentle agitation. Primary antibody concentrations and incubation times varied with the affinity of the antibody and the prevalence of the target epitope. For antibodies previously used in our lab for histologic immunofluorescence, we started with ten times the usual antibody concentration and 48 h of immersion then titrated the concentration based on imaging results. For novel antibodies, we started at a dilution strength

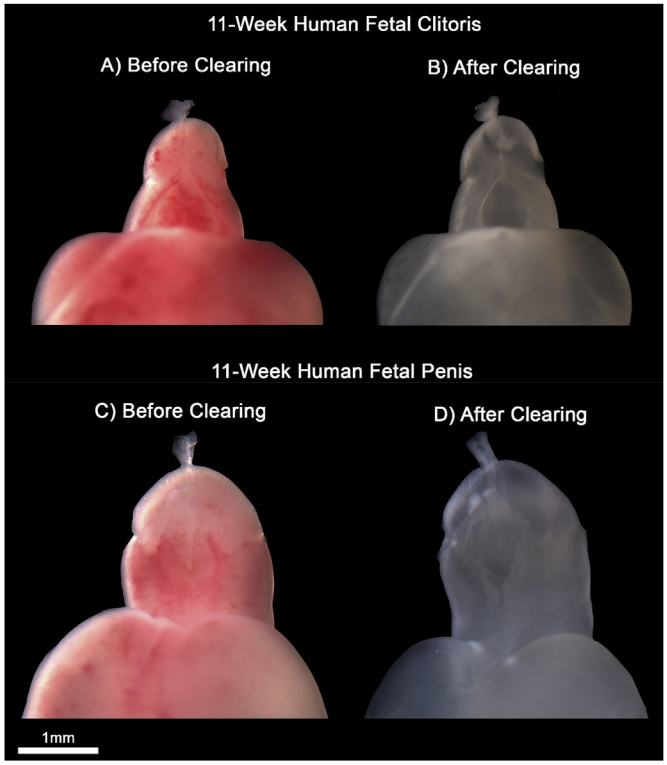

Fig. 5. 11-week human fetal clitoris (A, B) and penis (C, D) before and after clearing with the PAssive Clarity Technique (PACT). Proteins and nucleic acids were stabilized in an acrylamide-based hydrogel matrix, allowing for lipids to be gently dissolved by sodium dodecyl sulfate (SDS) to attain specimen transparency while preserving molecular targets for whole-mount immunostaining. *Top panel (clitoris) reproduced from Isaacson, D., J. Shen, M. Overland* et al., *Three-dimensional imaging of the developing human fetal urogenital-genital tract: Indifferent stage to male and female differentiation. Differentiation, 2018.* ***103****: p. 14–23.*

of 1:100.

After primary antibody incubation, we washed specimens for at least 24 h in PBS supplemented with 0.1% TWEEN® (Sigma-Aldrich, St. Louis, MO), a mild detergent, with 3–5 buffer changes to reduce non-specific binding and background fluorescence. Secondary antibody immersion was conducted in the same fashion as primary antibody immersion, with secondary antibodies conjugated to fluorophores matched to the species of each primary antibody. We diluted all secondary antibodies to a strength of 1:100 in blocking buffer and immersed specimens for 48 h. All containers were covered with foil to avoid photobleaching from ambient room light. Following secondary antibody treatment, specimens were again washed in PBS with TWEEN® for at least 24 h with 3–5 PBS changes.

2.6. Agarose embedding and refractive index matching

To suspend specimens at the level of microscope objectives, we embedded our specimens in transparent low-melting point agarose (Thermo Fisher Scientific, Waltham, MA). Once heated, low melting point agarose remains liquid until it reaches 25 °C, allowing for specimen immersion without the protein denaturation that occurs at higher temperatures. Low-melting point agarose is prepared via dilution in sterile water followed by heating on a hot plate, in a heating block or in a microwave until the agarose is fully dissolved and the solution is transparent. If the concentration of the low-melting point agarose is too low, the column holding the specimen will lack integrity. If the concentration is too high, it will interfere with laser transmission. We recommend starting with 2% low-melting point agarose and

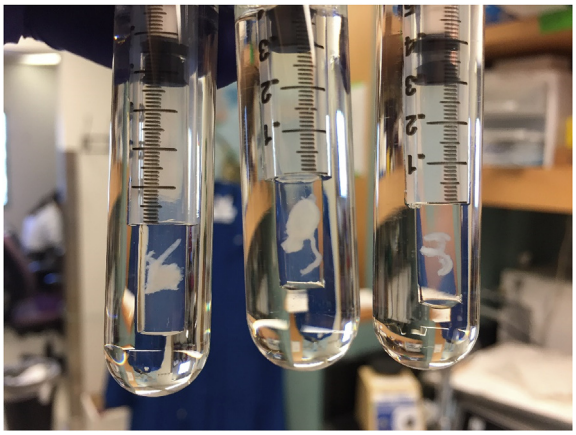

Fig. 6. Human fetal specimens embedded in low melting point agarose, pulled into 1 ml syringes and equilibrating in Refractive Index-Matching Solution (RIMS). From left, 9.5-week intact female pelvic organs (see Fig. 7), 12-week prostate and bladder (see Fig. 11) and 9-week female internal genital tract (see Fig. 12).

titrating based on results.

Once our low-melting point agarose cooled to about 30 °C, specimens were transferred into the liquid agarose solution and pulled into either a glass capillary tube or a 1 ml plastic syringe with the distal end cleanly removed with a razor blade (Fig. 6). It is important to leave a column of agarose of at least 15 mm above the specimen to allow for extrusion of the column into the chamber of the microscope for imaging. To optimize light passage through the agarose and the embedded specimen, the specimen must be allowed to equilibrate in Refractive Index-Matching Solution (RIMS). Our agarose-embedded specimens were allowed to cool in the capillary tube or syringe for at least 20 min or until solid. They were then extruded into a container filled with enough RIMS to cover the specimen (Fig. 6). The container was covered with foil and kept at room temperature for at least 24 h. Longer immersion times will improve refractive index-matching but at the risk of

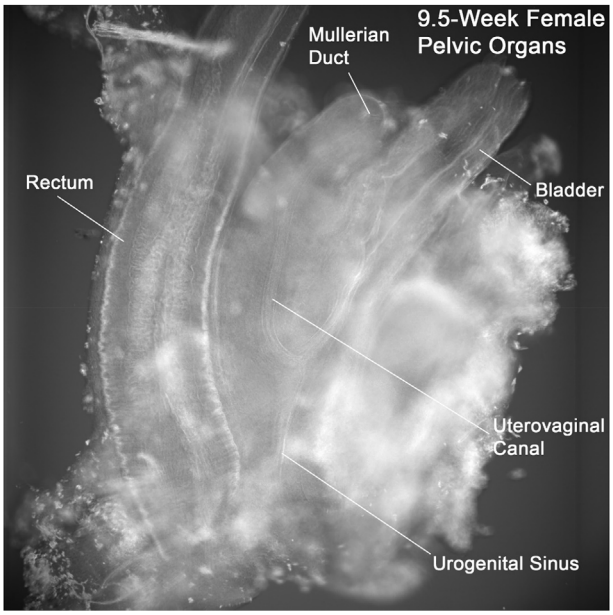

Fig. 7. 9.5-week intact human fetal pelvic organs visualized within LSFM device using transmitted infrared light from its LED light source. This view is used to finely orient the specimen for subsequent light sheet illumination and data capture. Distinct organs – rectum, Mullerian duct and bladder are visible. The junction of the nascent uterovaginal canal with the urogenital sinus is also visualized in this view.

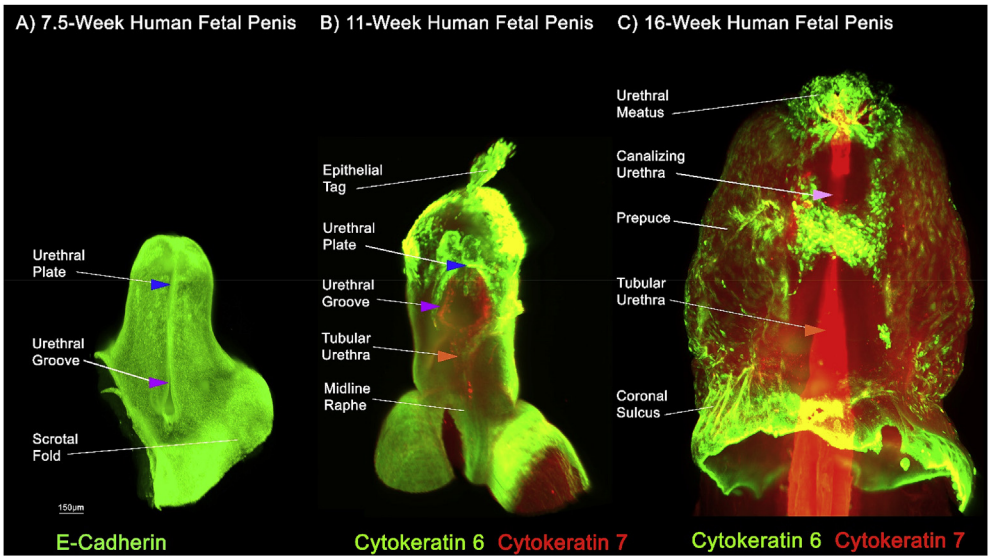

Fig. 8. Light sheet fluorescence microscopy images demonstrating development of the penile urethra at the ambisexual stage (A, 7.5 weeks), during active urethral canalization and fusion to form the urethra in the penile shaft (B, 11 weeks) and during direct canalization to form the mature urethra in the glans penis (C, 16 weeks). E-cadherin is expressed at epithelial surfaces in development, Cytokeratin 6 is expressed in the urethral plate and epidermis and Cytokeratin 7 is expressed in urothelium. *Reproduced from Isaacson, D., J. Shen, M. Overland* et al., *Three-dimensional imaging of the developing human fetal urogenital-genital tract: Indifferent stage to male and female differentiation. Differentiation, 2018.* ***103****: p. 14–23, with permission.*

microbial growth on the agarose.

RIMS can be made with various solutes (Treweek et al., 2015). We used Histodenz™ (Sigma-Aldrich, St. Louis, MO, USA) to optimize imaging performance as outlined by Treweek et al. (2015) (Treweek et al., 2015). To prepare our RIMS, we dissolved 40g of Histodenz™ in 30 ml of sterile 0.02M PBS. As the resultant solution was very viscous, we warmed it gently on a hot plate with a magnetic stir bar in a clean beaker to facilitate dissolution. This resulted in RIMS with a refractive index of n = 1.46 (Marx, 2014)' (Yang et al., 2014). As Histodenz™ is expensive, we reused each batch of RIMS multiple times over several months. Sodium azide added to the solution to reach a final concentration of 0.01% and storage of the solution at 4 °C helped reduce microbial growth over its lifetime.

2.7. Imaging

We imaged the depicted specimens on a light sheet Z.1 device (Carl Zeiss AG, Oberkochen, Germany), a commercially available single-plane illumination microscope (Strobl et al., 2017) using its 5x/0.16 detection objective and Zeiss's ZEN Microscope Software. Laser illumination and recording objectives acquire image data through a chamber inside the microscope which is filled with the same RIMS used to equilibrate specimens, ensuring a good refractive index match. Specimens were secured using the microscope's chamber adapters (designed to hold a glass capillary tube or 1 ml syringe) and lowered into the chamber using microscope controls.

For the specimen shown (Fig. 7), the orientation of the 1 ml syringe was coarsely guided by a digital camera external to the specimen chamber and then more finely with transmission contrast provided by infrared light-emitting diode (LED) illumination through the detection objective of the microscope. When the specimen was oriented with all structures of interest in view, we switched to fluorescence illumination with lasers set to the wavelengths of the target fluorophores (continuous mode). The light sheet Z.1 has five laser channels that can be added on separate tracks to illuminate up to five fluorophores. The Z.1 illuminates specimens using light sheets from two sides, thus left and right lasers were carefully aligned to the focal plane and to each other to ensure that structures were illuminated in the same plane. Zoom was adjusted to ensure inclusion of all structures of interest. Note that zooming out too far will result in vignetting, or loss of intensity and blurring of the corners of the image. Laser power was adjusted to a level providing good contrast and clear visualization of antibody-labeled structures. We imaged using the settings “dual side when experiment” and “online dual side fusion” in order to capture and subsequently merge images from both left and right lasers.

The microscope captures images via translation of the specimen along its Z axis, taking alternating images from the left and right sides and merging them to produce the final “Z-stack”. The imaging start and stop points along the Z axis are defined by the operator after navigating through the specimen in continuous mode. We defined these as the points just past the outer peripheries of the specimen to ensure it is fully imaged.

2.8. Post-processing

We used Imaris (Bitplane AG, Andor, Zurich, Switzerland) to reconstruct our Z-stacks into 3D datasets. In addition to taking screenshots and short videos navigating through the 3D model, Imaris allows for point-to-point and volume measurements as well as viewing slices of the model taken through any user-defined plane. Individual channels can be toggled on and off and their exposure levels and colors adjusted to create modified views of the sample.

2.9. Antibody removal and re-staining

Specimens can be cleared of bound antibody via re-immersion into 8% SDS in 1x PBS solution at 37 °C with gentle agitation as was performed in the initial clearing step. We recommend 24–72 h in solution depending on the size, density and degree of epithelization of the organ. The choice of re-immersion time is balanced between removing the previous antibodies while preserving the integrity of the specimen. Once cleared, the organ can then be washed in PBS, blocked, immunostained and imaged again. This is faster than starting with a fresh organ and, over time, can allow for comparison of many antigenic targets within the same specimen.

3. Results

3.1. External genital development

Fig. 8 traces the development of the penile urethra starting from the ambisexual stage of < 7.5 weeks (Fig. 8A) with the urethral groove at the level of the scrotal folds (purple arrow). In Fig. 8B, the distally canalizing urethral plate (blue arrow), open urethral groove (purple arrow) and proximally fused tubular urethra (orange arrow) of an 11-week specimen are seen. Cytokeratin 6 (K6, green) is expressed in basal and supra-basal cells of stratified epithelium comprising more superficial structures whereas Cytokeratin 7 (K7, red) highlights the

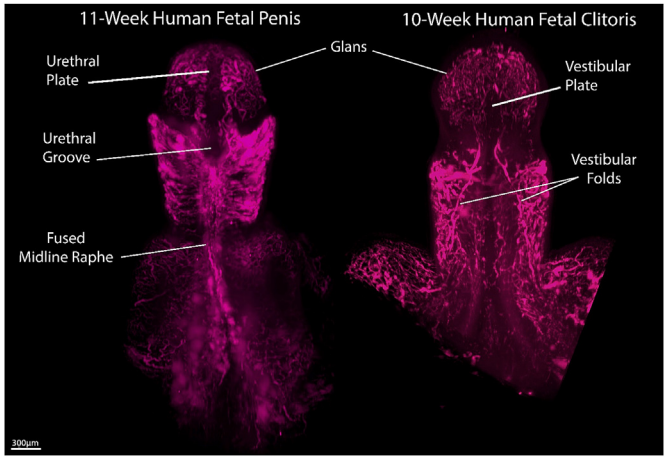

Fig. 9. Light sheet fluorescence microscopy images of 11-week human fetal penis (A) and 10-week human fetal clitoris (B) demonstrating nascent vasculature. Note the dense regions of vasculature on the ventral surface around the canalizing urethral groove and fused midline raphe of the penis. This observation has been confirmed by standard immunostaining of tissue sections (unpublished observations) The clitoris demonstrates dense vascularity around analogous regions of the clitoral shaft with large vessels running along the medial aspects of the vestibular folds. *Reproduced from Isaacson, D., J. Shen, M. Overland* et al., *Three-dimensional imaging of the developing human fetal urogenital-genital tract: Indifferent stage to male and female differentiation. Differentiation, 2018.* ***103****: p. 14–23, with permission.* See Supplemental Figs. 1 and 2 for videos of 3D models.

endodermal epithelium of the urethra. In conjunction, these double stains show progression of the nascent urethra in the process of canalization and fusion. Fig. 8C demonstrates formation of the nascent urethra directly through the urethral plate (pink arrow) in the glans during distal urethral development (16 weeks). This occurs in the absence of formation of a urethral groove. At all stages of penile development, the urethral plate is consistently highlighted by both E-cadherin and Cytokeratin 6. We believe that recent publication of this 11-week specimen represented the first whole-mount LSFM double stain demonstrating nascent expression of urethral urothelium in a developing human penis (Isaacson et al., 2018a). Similarly, the 16-week specimen was likely the first to demonstrate direct canalization of the developing human urethra through the glans penis (Liu et al., 2018).

Fig. 9 shows the vasculature of 11-week male (Fig 9A) and 10-week female (Fig. 9B) fetal genital tubercles. Analogous structures such as the developing glans penis and glans clitoris show similarly tortuous vessels. Likewise, the urethral and vestibular plate demonstrate an absence of vasculature.

The ventral aspects of the clitoral vestibular folds feature prominent vessels, analogous to the vascular density seen at the fused proximal midline raphe overlying the recently tubularized proximal penile urethra. These remain the only known whole-mount images demonstrating the vasculature of the developing human external genitalia. For videos rotating these specimens in 3D, see Supplemental Figs. 1 and 2.

Supplementary video related to this article can be found at https://doi.org/10.1016/j.diff.2019.09.006

3.2. Renal development

Fig. 10 shows an 11-week lobulated human fetal kidney double-stained to highlight ureteric bud epithelium expressing E-cadherin (Fig. 10A, red) and metanephric mesenchyme expressing HoxA11 (Fig. 10C, green) (Isaacson et al., 2018b). The resultant merged 3D image (Fig. 10B) demonstrates iterative bifid and trifid branching of the ureteric bud in interaction with distinct zones of condensed metanephric mesenchyme. We have used these specific double stains to demonstrate branching of the ureteric bud as early as 7 weeks of fetal age (data not shown). Supplemental Fig. 3 demonstrates the branching ureteric bud in 3D in a video taken while rotating through the model.

Supplementary video related to this article can be found at https://doi.org/10.1016/j.diff.2019.09.006

3.3. Bladder and prostate development

Fig. 11 illustrates the relationship between the nerves of the prostate and bladder along with budding morphology of the developing prostate in multiple views of a 12-week specimen. The nerves are stained with S-100 (green) and are visible running anterolateral to the prostate and lateral to the bladder in close relation with the ureterovesical junction. E-cadherin (red) highlights the elongating and branching prostatic buds, the ejaculatory ducts as well as the urethral urothelium and the trigone. Fig. 12 demonstrates the same 12-week specimen stained for E-cadherin (red, Fig. 12A) with the green S-100 fluorophore channel turned down. It was cleared with SDS and re-stained with anti-alpha smooth muscle actin (α-SMA, red, Fig. 12B). The trigone, ureteral epithelium and prostatic buds are again highlighted by E-cadherin. α-SMA is expressed in the smooth muscle comprising the detrusor of the bladder and circumferentially around both the ureters and the capsule of the prostate, expression patterns consistent with prior histologic studies of α-SMA in the human prostate (Cunha et al., 2018). Both E-cadherin and α-SMA primary antibodies were labeled with the same 555 nm Goat Anti-Mouse IgG Heavy + Light chain secondary antibody (Alexa Fluor ® 555, Abcam, Cambridge, UK). The absence of prostatic bud or ureteral epithelial staining in Fig. 12B therefore demonstrates successful clearing and re-staining.

3.4. Female internal genital development

Fig. 13 shows the female reproductive tract at approximately 9.5 weeks fetal age. E-cadherin (Fig. 13A, C, red) faintly highlights the paired Mullerian ducts, which have fused at midline to form the uterovaginal canal as well as the paired Wolffian ducts and the point at which both sets of ducts meet the urogenital sinus. Decreasing the intensity of the red laser channel allows for visualization of Pax2 (Fig. 13B, green) which selectively highlights Mullerian epithelium. For better visualization of this relationship in 3D, see the video in Supplemental Fig. 4.

Supplementary video related to this article can be found at https://doi.org/10.1016/j.diff.2019.09.006

3.5. Male gonadal development

The human fetal testis presented in Fig. 14 was identified in the pelvis of a 14.5 week male fetal specimen. It was stained with E-cadherin (green) and anti-Mullerian hormone (AMH, blue). The epididymis and vas deferens are identified via E-cadherin staining whereas AMH is strongly expressed in Sertoli cells and highlights developing fetal seminiferous tubules (Rajpert-De Meyts et al., 1999).

4. Discussion

Since the advent of Gustav Born's method of stacking and melting wax plates, advances in three-dimensional reconstruction of human embryonic and fetal organs have enabled leaps in our understanding of their development. Recent work from our group using optical projection tomography (OPT) challenged prior dogma regarding mechanisms of development of the human penile urethra and analogous structures in the clitoris. We demonstrated that two sequential distal canalization and proximal fusion processes are involved rather than a single fusion process of paired urethral folds (Li et al., 2015; Overland et al., 2016; Shen et al., 2016). Prior to our use of 3D reconstruction, this

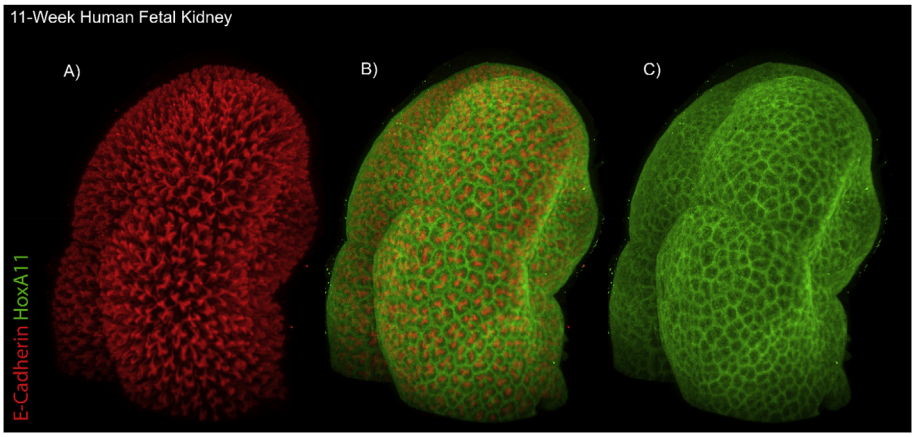

Fig. 10. Light sheet Fluorescence Microscopy (LSFM) image of a lobulated 11-week human fetal kidney stained with anti-E-Cadherin (A, red) and anti-HoxA11 (C, green) demonstrating sites of interaction of ureteric bud epithelium (C) with overlying HoxA11-expressing metanephric mesenchyme. *Reproduced from: Isaacson, D., J. Shen, D. McCreedy* et al., *Lightsheet fluorescence microscopy of branching human fetal kidney. Kidney Int, 2018.* ***93****(2): p. 525, with permission.* See Supplemental Fig. 3 for video of 3D model. (For interpretation of the references to color in this figure legend, the reader is referred to the Web version of this article.)

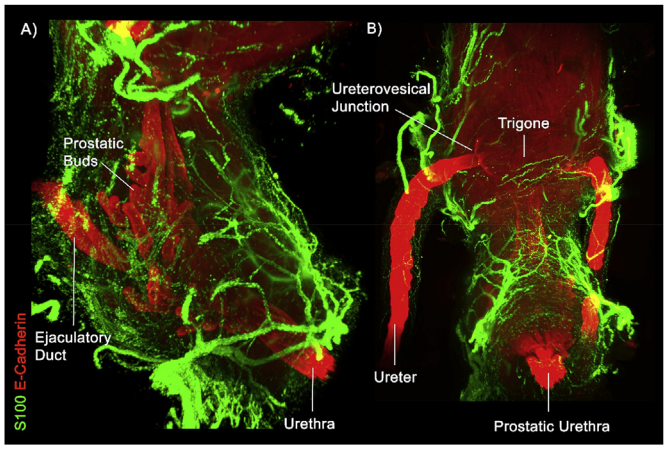

Fig. 11. Lateral (A) and anterior-posterior (B) light sheet fluorescence microscopy images of 12-week human fetal prostate and bladder stained with E-cadherin (red) and S-100 (green). E-cadherin highlights the epithelial surfaces of prostate buds, ejaculatory ducts, ureters and the prostatic urethra. S-100 selectively stains nerves which are seen running anterolateral to the prostate and lateral to the bladder in close relation to the ureterovesical junction. (For interpretation of the references to color in this figure legend, the reader is referred to the Web version of this article.)

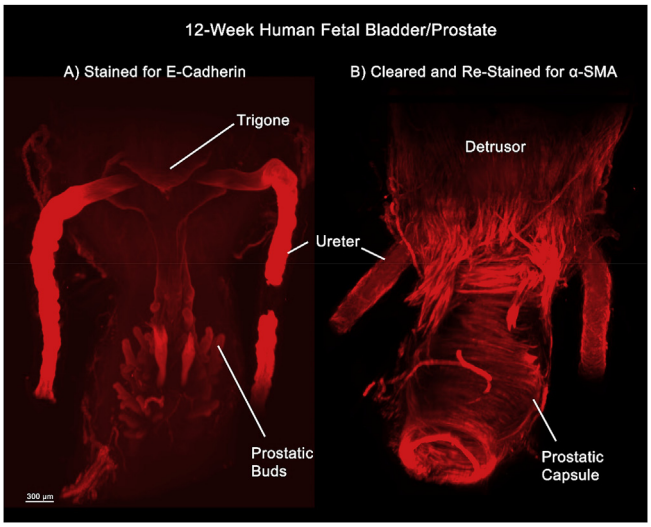

Fig. 12. Light sheet fluorescence microscopy images of the same 12-week human fetal bladder/prostate (Fig. 11) following initial staining for E-cadherin, clearing in SDS and re-staining for α-SMA. Prostatic buds, trigone and ureteral epithelium are again highlighted by E-cadherin (A). Smooth muscle fibers of the detrusor, ureter and prostatic capsule express α-SMA (B). The absence of prostatic bud and ureteral epithelial fluorescence in (B) despite the use of a secondary antibody with an identical fluorophore wavelength demonstrates successful clearing and re-staining.

observation had eluded us despite decades of examination of serial histologic sections.

Despite these advances, differential protein localization within developing human urogenital organs remains poorly characterized in three dimensions. Limitations of studies applying older 3D reconstruction techniques such as histology, confocal microscopy, scanning electron microscopy and OPT include the following: 1) slow speeds of data acquisition, 2) the inability to reuse previously imaged organs necessitating comparisons between unrelated specimens of similar age and 3) a lack of quantitative and statistical analyses. These barriers, coupled with limited access to fetal urogenital tissue and regulations preventing its use in research, represented substantial hurdles in performing large studies. The application of LSFM/SPIM outlined in this work addresses all of these shortcomings. Our specimens were imaged in minutes per specimen, enabling batch preparation of specimens and the creation of up to ten 3D models with up to three simultaneous immunostains in a single microscopy session. We have successfully cleared specimens of previous immunolabels, prepared them with new sets of antibodies and re-imaged them without the need to acquire new specimens for each run. Data analysis software enables objective measurement of protein localization and co-localization analyses between multiple antigenic targets within the same specimen. Ideal cross-sectional studies applying LSFM/SPIM would involve the collection of the ontogeny of specific urogenital organs throughout developmental time and of multiple specimens at the same developmental age. With batch preparation and reuse of specimens, the number of antigenic targets and specimens analyzed would be exponentially larger than current studies and could incorporate rigorous quantitative methods. While comparison of antigenic targets within the same clearing and re-staining cycle is likely valid, further study should evaluate specimen integrity through multiple rounds of clearing and re-staining to determine if image datasets can be successfully re-aligned without distortion.

In addition to applications in descriptive and cross-sectional work, LSFM/SPIM could be a powerful tool to study the effects of various hormones, growth factors and environmental toxicants on developing human urogenital organs. We recently described our renal subcapsular xenografting model of human urethral development (Isaacson et al., 2017). In this model system, we successfully grew human embryonic and fetal genital tubercles under the kidney capsules of athymic nude mice. This enabled us to study differentiation of the human genital tubercle in varying hormonal environments. LSFM/SPIM imaging should be applied to quantify and compare changes in expression of

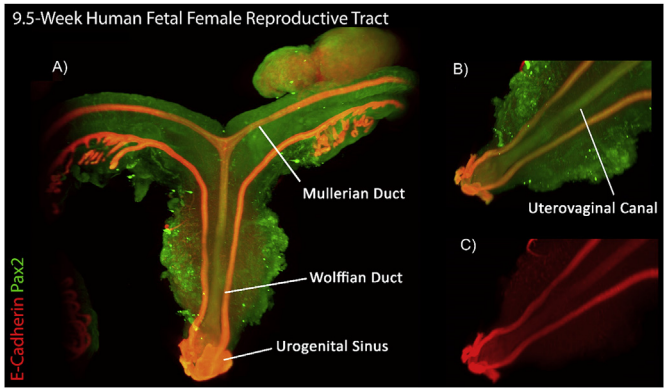

Fig. 13. Light sheet Fluorescence Microscopy images of 9.5-week human fetal female reproductive tract stained with E-cadherin (red) and Pax2 (green). Fusing Mullerian ducts and paired Wolffian ducts are both visualized terminating at the urogenital sinus (A). Pax2 selectively highlights the uterovaginal canal (B) while E-cadherin staining is absent in Mullerian-derived structures (C). *Adapted from: Cunha G, Robboy S, Kurita T, Isaacson D* et al. *Development of the human female reproductive tract. Differentiation, 2018.* ***103****: p 46–65, with permission.* See Supplemental Fig. 4 for video of 3D model. (For interpretation of the references to color in this figure legend, the reader is referred to the Web version of this article.)

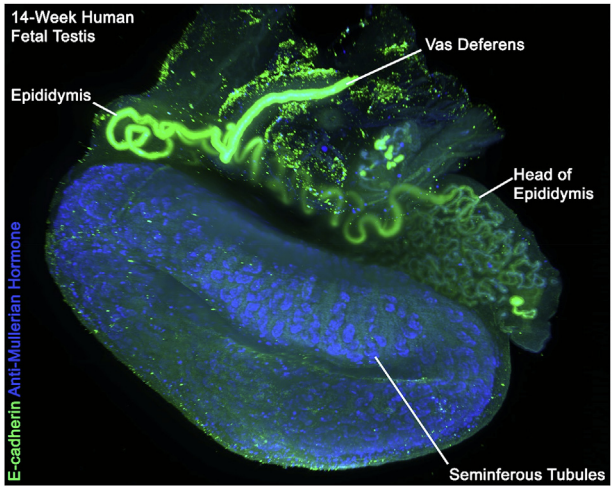

Fig. 14. Light sheet Fluorescence Microscopy image of 14.5-week human fetal testis stained with E-cadherin (green) and anti-Mullerian hormone (AMH, blue). E-cadherin highlights the epithelium of the vas deferens and epididymis. AMH is strongly expressed in Sertoli cells, highlighting developing fetal seminiferous tubules. (For interpretation of the references to color in this figure legend, the reader is referred to the Web version of this article.)

relevant genes such as the androgen receptor (AR) and estrogen receptor alpha (ER-α) in xenografts grown in varying environments.

Finally, contemporary light sheet devices allow for imaging of live specimens over time within integrated chambers allowing for incubation and gas exchange. This has enabled researchers to image real-time biological phenomena such as flow dynamics in naturally optically transparent zebrafish embryonic hearts (Fei et al., 2016). *Ex vivo* organ culture methods have been used for decades in developmental biology (McClelland and Bowles, 2016). LSFM/SPIM of cultured murine or human embryonic genital tubercles could illuminate real-time external genital development in controlled environments rather than simply at single points in development.

5. Conclusions

In this article we have outlined a technique for preparing and imaging human fetal urogenital specimens using light sheet fluorescence microscopy. We have applied this method to highlight target proteins at high resolution within human fetal organs throughout the urinary and genital systems. This work enables a new generation of study to elucidate both normal development and the genetic basis of congenital urogenital anomalies.

Funding sources

This work was supported by the National Institutes of Health [R01 DK058105/DK/NIDDK (LB), K12 DK083021/DK/NIDDK (AS)]; The American Urological Association/ Urology Care Foundation Herbert Brendler, MD Research Fellowship (DI); The Alpha Omega Alpha Honor Medical Society Carolyn L. Kuckein Medical Student Research Fellowship (DI); and a Pathways to Discovery Project Grant from the University of California, San Francisco (DI).

Abbreviations Used

α-SMA	Alpha smooth muscle actin
3D	Three-dimensional
3DISCO	3D Imaging of Solvent-Cleared Organs
AMH	Anti-Mullerian hormone
AR	Androgen receptor
ER-α	Estrogen receptor alpha
FAD	Flavin adenine dinucleotide
IRB	Institutional review board
K6, K7	Cytokeratin 6, Cytokeratin 7
LED	Light-emitting diode
LSFM	Light sheet fluorescence microscopy
NADH	Nicotinamide adenine dinucleotide
OPT	Optical projection tomography
PACT	PAssive CLARITY Technique
PARS	Perfusion-Assisted Release in Situ
PBS	Phosphate buffered saline
PCR	Polymerase chain reaction
PFA	Paraformaldehyde
RIMS	Refractive index-matching solution
RPMI	Roswell Park Memorial Institution [medium]
SDS	Sodium dodecyl sulfate
UCSF	University of California, San Francisco

References

Adams, M.W., Loftus, A.F., Dunn, S.E., et al., 2015. Light sheet fluorescence microscopy (LSFM). Curr Protoc Cytom 71, 12 37 1–15.
Andersson, H., Baechi, T., Hoechl, M., et al., 1998. Autofluorescence of living cells. J. Microsc. 191 (Pt 1), 1–7.
Belle, M., Godefroy, D., Couly, G., et al., 2017. Tridimensional visualization and analysis of early human development. Cell 169 (1), 161–173 e12.
Born, G., 1883. Die plattenmodellirmethode. Arch. Mikrosk. Anat. 22, 584–599.
Chung, K., Wallace, J., Kim, S.Y., et al., 2013. Structural and molecular interrogation of intact biological systems. Nature 497 (7449), 332–337.
Cunha, G., Overland, M., Li, Y., et al., 2016. Methods for studying human organogenesis. Differentiation 91 (4–5), 10–14.
Cunha, G.R., Vezina, C.M., Isaacson, D., et al., 2018. Development of the human prostate. Differentiation 103, 24–45.
Dodt, H.U., Leischner, U., Schierloh, A., et al., 2007. Ultramicroscopy: three-dimensional visualization of neuronal networks in the whole mouse brain. Nat. Methods 4 (4), 331–336.
Drey, E.A., Kang, M.S., McFarland, W., et al., 2005. Improving the accuracy of fetal foot length to confirm gestational duration. Obstet. Gynecol. 105 (4), 773–778.
Erturk, A., Bradke, F., 2013. High-resolution imaging of entire organs by 3-dimensional imaging of solvent cleared organs (3DISCO). Exp. Neurol. 242, 57–64.
Erturk, A., Becker, K., Jahrling, N., et al., 2012. Three-dimensional imaging of solvent-cleared organs using 3DISCO. Nat. Protoc. 7 (11), 1983–1995.
Fei, P., Lee, J., Packard, R.R., et al., 2016. Cardiac light-sheet fluorescent microscopy for multi-scale and rapid imaging of architecture and function. Sci. Rep. 6, 22489.
Hama, H., Kurokawa, H., Kawano, H., et al., 2011. Scale: a chemical approach for fluorescence imaging and reconstruction of transparent mouse brain. Nat. Neurosci. 14 (11), 1481–1488.
Hama, H., Hioki, H., Namiki, K., et al., 2015. ScaleS: an optical clearing palette for

biological imaging. Nat. Neurosci. 18 (10), 1518–1529.
Hockendorf, B., Lavis, L.D., Keller, P.J., 2014. Making biology transparent. Nat. Biotechnol. 32 (11), 1104–1105.
Hopwood, N., 1999. Giving body" to embryos. Modeling, mechanism, and the microtome in late nineteenth-century anatomy. Isis 90 (3), 462–496.
Huisken, J., Stainier, D.Y., 2009. Selective plane illumination microscopy techniques in developmental biology. Development 136 (12), 1963–1975.
Huisken, J., Swoger, J., Del Bene, F., et al., 2004. Optical sectioning deep inside live embryos by selective plane illumination microscopy. Science 305 (5686), 1007–1009.
Isaacson, D., Shen, J., Cao, M., et al., 2017. Renal Subcapsular xenografing of human fetal external genital tissue - a new model for investigating urethral development. Differentiation 98, 1–13.
Isaacson, D., Shen, J., Overland, M., et al., 2018a. Three-dimensional imaging of the developing human fetal urogenital-genital tract: Indifferent stage to male and female differentiation. Differentiation 103, 14–23.
Isaacson, D., Shen, J., McCreedy, D., et al., 2018b. Lightsheet fluorescence microscopy of branching human fetal kidney. Kidney Int. 93 (2), 525.
Li, Y., Sinclair, A., Cao, M., et al., 2015. Canalization of the urethral plate precedes fusion of the urethral folds during male penile urethral development: the double zipper hypothesis. J. Urol. 193 (4), 1353–1359.
Liu, X., Liu, G., Shen, J., et al., 2018. Human glans and preputial development. Differentiation 103, 86–99.
Marx, V., 2014. Microscopy: seeing through tissue. Nat. Methods 11 (12), 1209–1214.
McClelland, K.S., Bowles, J., 2016. Culturing murine embryonic organs: pros, cons, tips and tricks. Differentiation 91 (4–5), 50–56.
Menter, P. Acrylamide polymerization - a practical approach. Bio-Rad Tech Note 1156.
Overland, M., Li, Y., Cao, M., et al., 2016. Canalization of the vestibular plate in the absence of urethral fusion characterizes development of the human clitoris: the single zipper hypothesis. J. Urol. 195 (4 Pt 2), 1275–1283.
Rajpert-De Meyts, E., Jorgensen, N., Graem, N., et al., 1999. Expression of anti-Mullerian hormone during normal and pathological gonadal development: association with differentiation of Sertoli and granulosa cells. J. Clin. Endocrinol. Metab. 84 (10), 3836–3844.
Reynaud, E.G., Peychl, J., Huisken, J., et al., 2015. Guide to light-sheet microscopy for adventurous biologists. Nat. Methods 12 (1), 30–34.
Richardson, D.S., Lichtman, J.W., 2015. Clarifying tissue clearing. Cell 162 (2), 246–257.
Santi, P.A., 2011. Light sheet fluorescence microscopy: a review. J. Histochem. Cytochem. 59 (2), 129–138.
Shen, J., Overland, M., Sinclair, A., et al., 2016. Complex epithelial remodeling underlie the fusion event in early fetal development of the human penile urethra. Differentiation 92 (4), 169–182.
Siedentopf, H., Zsigmondy, R., 1903. Über sichtbarmachung und groessenbestimmung ultramikroskopischer teilchen, mit besonderer anwendung auf goldrubinglaesern. Ann. Phys. 10, 1–39.
Strobl, F., Schmitz, A., Stelzer, E.H.K., 2017. Improving your four-dimensional image: traveling through a decade of light-sheet-based fluorescence microscopy research. Nat. Protoc. 12 (6), 1103–1109.
Tomer, R., Ye, L., Hsueh, B., et al., 2014. Advanced CLARITY for rapid and high-resolution imaging of intact tissues. Nat. Protoc. 9 (7), 1682–1697.
Treweek, J.B., Chan, K.Y., Flytzanis, N.C., et al., 2015. Whole-body tissue stabilization and selective extractions via tissue-hydrogel hybrids for high-resolution intact circuit mapping and phenotyping. Nat. Protoc. 10 (11), 1860–1896.
Yang, B., Treweek, J.B., Kulkarni, R.P., et al., 2014. Single-cell phenotyping within transparent intact tissue through whole-body clearing. Cell 158 (4), 945–958.